


Orbitally selective Mott phase in electron-doped twisted transition metal-dichalcogenides: A possible realization of the Kondo lattice model

Amir Dalal  and Jonathan Ruhman 

*Department of Physics, Bar-Ilan University, 52900, Ramat Gan, Israel
and Center for Quantum Entanglement Science and Technology, Bar-Ilan University, 52900, Ramat Gan Israel*

 (Received 30 March 2021; revised 7 November 2021; accepted 9 November 2021; published 10 December 2021)

Moiré superpotentials in two-dimensional materials allow unprecedented control of the ratio between kinetic and interaction energy. By this they pave the way to study a wide variety of strongly correlated physics under a new light. In particular, the transition-metal dichalcogenides (TMDs) are promising candidate “quantum simulators” of the Hubbard model on a triangular lattice. Indeed, Mott and generalized Wigner crystals have been observed in such devices. Here we theoretically propose to extend this model into the multiorbital regime by focusing on electron-doped systems at filling higher than 2. As opposed to hole bands, the electronic bands in TMD materials include two, nearly degenerate species, which can be viewed as two orbitals with different effective mass and binding energy. Using realistic band-structure parameters and a slave-rotor mean-field theory, we find that an orbitally selective Mott (OSM) phase can be stabilized over a wide range of fillings, where one band is locked in a commensurate Mott state, while the other remains itinerant with variable density. This scenario thus realizes the basic ingredients in the Kondo lattice model: a periodic lattice of localized magnetic moments interacting with metallic states. We also discuss possible experimental signatures of the OSM state.

DOI: [10.1103/PhysRevResearch.3.043173](https://doi.org/10.1103/PhysRevResearch.3.043173)

I. INTRODUCTION

Experiments in van der Waals materials have convincingly demonstrated the power of moiré superlattices as a tool to tune the strength of electronic correlations. Following the theoretical prediction [1], a wide variety of strongly correlated phenomena was experimentally observed [2–14]. The Dirac dispersion, characterizing the unperturbed electronic states in graphene, leads to topologically nontrivial flat bands [15,16] with large Wannier orbitals [15,17,18], from which these correlated states emerge.

In contrast, semiconducting transition-metal dichalcogenides (TMDs) subject to moiré potentials are expected to have a simpler microscopic picture. The low-energy physics is captured by a Hubbard model on a triangular lattice [19,20]. Mott insulators and generalized Wigner crystals have been experimentally observed [21–24], as well as possible indications of superconductivity [21]. The relative simplicity of their microscopic starting point makes the TMD moiré devices prime candidates for condensed-matter “quantum simulators” of the Hubbard model.

A canonical model that is both of great fundamental interest to quantum condensed matter, and has not yet been realized in moiré devices, is the Kondo lattice model [25]. Its main ingredients are a lattice of localized moments coupled

to a Fermi liquid of itinerant electrons. The main coupling between these two degrees of freedom is spin exchange. The case where the strongest exchange mechanism is antiferromagnetic is understood to be the minimal model that captures the low-energy physics of many rare-earth compounds, known as *heavy-fermion materials* [26,27]. When the dominant exchange is the Hund’s coupling between the local and itinerant orbitals, the coupling is ferromagnetic. Such a scenario was discussed in the context of the *orbitally selective Mott* (OSM) phase [28,29].

Materials that host coexisting itinerant and localized states exhibit a plethora of exotic phases such as heavy-Fermi liquids, metallic magnets, high- T_c superconductors, and non-Fermi liquids [28–40]. However, what makes them especially interesting is the existence of quantum phase transitions, where the lattice of local moments melts into a metallic state [24,30,33,36,39,41–43]. Such a transition is not captured by the Ginzburg-Landau paradigm, because it must include a whole Fermi surface that emerges at the quantum critical point [34,37,40]. What controls the different ground states, and the nature of the quantum critical point separating them, is still debated. However, the comparison between theory and experiment becomes challenging due to the complex structure of the materials which realize this physics. For this reason, a controlled experimental realization of such a minimal model is highly desirable.

In this paper we explore the conditions under which TMDs subject to a moiré potential can host a state of coexisting itinerant and localized electrons known as the OSM state [29,40,45]. We first argue that the miniband structure of *electron-doped* TMD moiré devices can potentially host multiple flat bands, which can be simultaneously at a state of

Published by the American Physical Society under the terms of the Creative Commons Attribution 4.0 International license. Further distribution of this work must maintain attribution to the author(s) and the published article’s title, journal citation, and DOI.

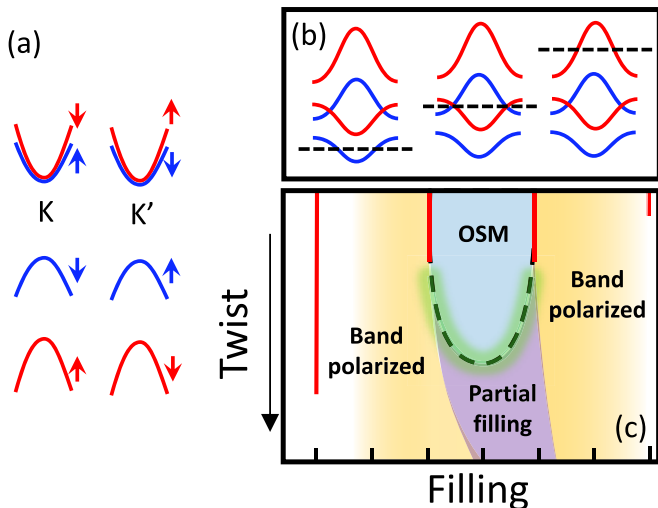


FIG. 1. (a) Schematic band structure of a single-layer TMD near the K and K' points. While the hole Bloch bands have a large spin-orbit coupling splitting, the electron bands are nearly degenerate (red and blue indicate different Bloch bands, which we refer to as “species”). (b) With a moiré potential the electron bands form multiple flat minibands that can overlap in energy space and be simultaneously at partial filling. (c) Schematic phase diagram arising from our slave-rotor mean-field analysis. A charge localized state of one species can coexist with a Fermi-liquid state of the other, which is known as the orbitally selective Mott (OSM) state. Inside the region marked by the dashed black line the essential ingredients of a Kondo lattice model are realized. The red lines indicate correlated insulating states.

partial filling. This is mainly because of the relatively small spin-orbit splitting of the bare conduction bands around the K and K' points [44] [see Fig. 1(a)]. We consider the situation where such minibands are induced in one layer by another “inactive” layer in a heterogeneous structure [19]. For example, two prototypical bilayers we consider are WS_2/WSe_2 , where the effects of spin-orbit splitting on the conduction bands are small but noticeable, and $\text{MoS}_2/\text{MoSe}_2$, where the splitting is negligible. In both cases the sulfur-based compounds are where the electronic states reside, and the selenium-based layers take the role of the “inactive” layer that induces the moiré potential. Using a slave-rotor mean-field approximation [46–48], which was recently used in the context of twisted bilayer graphene [49], we study a simplified on-site interaction Hubbard model. We identify the emergence of the OSM state at fillings surrounding $n = 4$ or $n = 2$ (depending on the strength of spin-orbit coupling). In this phase one species is in a Mott state while the other species is partially filling one of its minibands [see Figs. 1(b) and 1(c)].

II. MODEL HAMILTONIAN

The two lowest Bloch bands above the band gap, which we denote here as species $\tau = a, b$, have nearly degenerate band minima in the vicinity of each valley, K and K' [44] (see Fig. 2). Due to spin-orbit coupling they are split and assume different effective masses. As mentioned above, this splitting is significantly smaller compared with the equivalent splitting

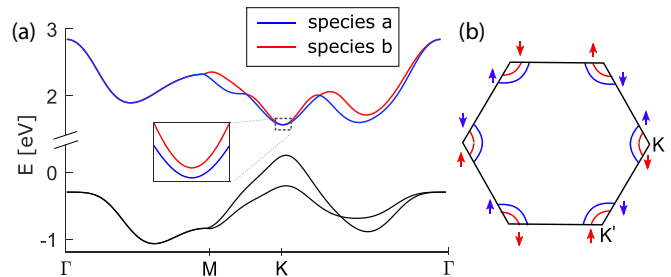


FIG. 2. (a) Typical dispersion of the two lowest Bloch bands of the conduction band in a bare single-layer TMD obtained from the tight-binding model [44]. Near the K and K' points the bands are approximately parabolic and assume a small splitting due to spin-orbit coupling in the second order (see inset), where each band can accommodate two electrons, one at each valley. (b) Upon lightly doping the system, two Fermi pockets of opposite spin orientation form around each high-symmetry point, corresponding to the two Bloch bands.

in the valence band. Nonetheless, the spin projection along z remains a good quantum number up to second order in perturbation theory. As usual, we obtain an additional valley degree of freedom by expanding the momentum around K and K' . Note, however, that spin-orbit coupling slaves spin to valley within a given Bloch band. We therefore denote the additional degree of freedom by its spin as follows: For the lower Bloch band $\tau = a$, the state $\sigma = \uparrow$ and $\sigma = \downarrow$ corresponds to a valley K and K' , respectively. On the other hand, for the higher Bloch band $\tau = b$, the state $\sigma = \uparrow$ and $\sigma = \downarrow$ correspond to a valley K' and K , respectively. The resulting Hamiltonian (up to quadratic order in deviation from the high-symmetry points), is given by

$$\mathcal{H}_0 = \sum_{k\tau\sigma} \left(\Delta_\tau + \frac{k^2}{2m_\tau} \right) c_{k\tau\sigma}^\dagger c_{k\tau\sigma}, \quad (1)$$

where Δ_τ and m_τ are the species-dependent band minimum and mass, respectively. The values are listed in Table I.

In principle, the Fermi surfaces surrounding the K and K' points (in terms of the momentum relative to these points) are nondegenerate except for six high-symmetry lines. However, as a result of the parabolic band approximation, used in Eq. (1), the Fermi surfaces are spherically symmetric and are thus doubly degenerate everywhere (the degeneracy corresponds to the spin index σ). This reflects an emergent $\text{SU}(2)$ symmetry of each species [19].

TABLE I. The effective mass and spin-orbit splitting near the conduction-band minima of the high-symmetry points K and K' for different TMD single layers (taken from Ref. [44]). Here $\Delta = \Delta_b - \Delta_a$ is the spin-orbit splitting between the bands.

	m_a/m_e	m_b/m_e	Δ (meV)
MoS_2	0.45	0.51	3
MoSe_2	0.51	0.61	21
WS_2	0.40	0.30	29
WSe_2	0.44	0.31	36

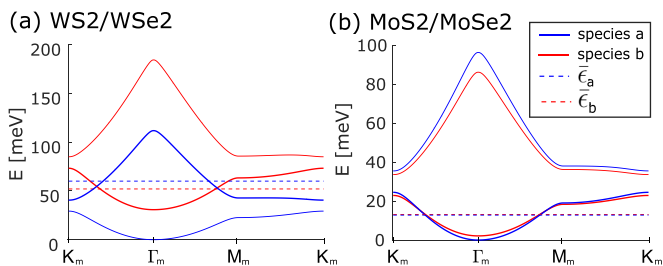


FIG. 3. The two lowest minibands of the two species near the conduction-band minima resulting from a moiré potential of angle $\theta_M = 3^\circ$ and depth $V_0 = 15$ meV. The dashed lines indicate the average band energies, $\bar{\epsilon}_\tau$ (see text). In this paper we focus on the lowest pair of such minibands that *overlap* in energy space. (a) For WS_2/WSe_2 this pair includes the lowest miniband of species *b* and the first excited band of species *a*. (b) For $\text{MoS}_2/\text{MoSe}_2$ the SOC is very weak and the miniband structure is nearly degenerate for all minibands. Therefore, for this material we consider the lowest miniband for both Bloch bands.

In this paper we consider two prototypical TMD bilayers, WS_2/WSe_2 and $\text{MoS}_2/\text{MoSe}_2$. In both cases the band alignment properties are such that the charge carriers reside on the sulfur-based side of the bilayer upon electronic doping. Thus the selenium-based layers are inactive and only induce the moiré potential. In the case of $\text{MoS}_2/\text{MoSe}_2$ spin-orbit coupling is very weak and consequently the masses m_τ and band minimum points Δ_τ in Eq. (1) are almost identical. In the case of WS_2/WSe_2 , the effects of spin-orbit coupling are more noticeable, such that $m_b/m_a \approx 0.75$ and $\Delta_b - \Delta_a = 30$ meV.

We now turn to consider the influence of a moiré potential on the band structure close to the bottom of the conduction bands $\tau = a, b$. We follow Refs. [19] and [20]. The induced potential is given by

$$\mathcal{H}_M = \sum_{j\tau k\sigma} V_0(\mathbf{G}_j) c_{\mathbf{k}+\mathbf{G}_j\tau\sigma}^\dagger c_{k\tau\sigma}, \quad (2)$$

where $\mathbf{G}_j = \hat{R}(j\frac{\pi}{3})(4\pi/\sqrt{3}a_M\hat{x})$, $j = 0, \dots, 5$ are the six shortest reciprocal lattice vectors of the moiré superlattice. $a_M = a/\theta_M$ is the moiré lattice constant, and $\theta_M = \sqrt{\delta^2 + \theta^2}$ is the effective twist angle. Here δ is the lattice mismatch, and θ accounts for any additional twist. We take the strength of the potential to be $V_0 = 15$ meV for both bilayers.

The parabolic Hamiltonian Eq. (1) together with the moiré potential Eq. (2) are diagonalized using a nearly-free-electron approximation truncated at the level of 19 bands (third nearest neighbor in reciprocal space).

In Fig. 3 we plot the two lowest minibands of each species using realistic parameters for the bilayers. In panel (a) we show that for the strongly spin-orbit-coupled bilayer, WS_2/WSe_2 , the lowest miniband of species *b*, overlaps with the first remote miniband of species *a*. On the other hand, in panel (b) we show that for the weakly spin-orbit-coupled bilayer, $\text{MoS}_2/\text{MoSe}_2$, the minibands of the two species are almost identical. In this case the two lowest minibands (and the two first excited bands) overlap in energy.

We will be interested in the physics arising from partially filling two different minibands simultaneously. Therefore, from here on we will focus exclusively on the *lowest pair* of

minibands that overlap in energy space corresponding to the two Bloch bands $\tau = a, b$. The miniband Hamiltonian then assumes the form

$$\mathcal{H}_{mb} = \sum_{k\tau\sigma} \xi_{k\tau} \psi_{k\tau\sigma}^\dagger \psi_{k\tau\sigma}. \quad (3)$$

However, we still define the density in units of *total filling*, starting from the bottom of the conduction band. Consequently, for WS_2/WSe_2 [Fig. 3(a)] the relevant range of filling is $n \in [2, 6]$, where the lowest miniband of species *a* is already *completely filled* and contributes a background charge of 2. This situation is also depicted in the center of panel (b) in Fig. 1. On the other hand, for $\text{MoS}_2/\text{MoSe}_2$ the two lowest minibands of each species overlap and therefore we focus on the range of filling $n \in [0, 4]$.

The second ingredient in our model is the interaction. We consider an on-site repulsion of the form

$$\mathcal{H}_I = \frac{U}{2} \sum_i (\eta \delta n_{ia} + \delta n_{ib})^2, \quad (4)$$

where $\delta n_\tau = \sum_\sigma \psi_{\tau\sigma}^\dagger \psi_{\tau\sigma} - 1$ is the density operator in particle-hole symmetric form [50]. η is a phenomenological parameter, which accounts for the possible difference in the Wannier-orbital spread of the species. When the lowest miniband of species *b* overlaps with the first remote miniband of *a* [Fig. 3(a)], the spread of the Wannier orbital of the latter is expected to be wider than that of the former. Consequently, electrons in miniband *a* will have a weaker Coulomb repulsion, corresponding to $\eta < 1$. On the other hand, when the overlapping minibands are both the first flat band [Fig. 3(b)], the interactions are expected to be roughly equal and $\eta = 1$. We consider a constant interaction U of moderate strength, which corresponds to the estimate of Ref. [19] with a large dielectric constant $\kappa \approx 5$ [51,52].

III. SLAVE-ROTOR MEAN-FIELD ANALYSIS

We now turn to study the ground state of the Hamiltonian Eqs. (3) and (4). In particular, we are interested to understand whether a Mott state of one of the species can be stabilized over a finite density range, where the other band remains metallic. To this end, we employ the slave-rotor mean-field theory [46–48]. It consists of decomposing the field operators into bosonic rotors multiplied by neutral spinon operators $\psi_{i\tau\sigma} = e^{-i\theta_{i\tau}} f_{i\tau\sigma}$. The respective density operator of each species, which are conjugates of the phases above, are then represented by angular momentum operators $\hat{L}_{i\tau} = -i\partial/\partial\theta_{i\tau}$, subject to the *local* constraint $\hat{L}_{i\tau} = f_{i\tau}^\dagger f_{i\tau} - 1$, where the sum over spin is implicit.

The above decomposition allows for a mean-field treatment of the Mott transition [46]. The corresponding “order parameter” is the quasiparticle weight $Z_\tau = |\langle e^{i\theta_\tau} \rangle|^2$. When the rotor fields are pinned $Z_\tau \neq 0$, resulting in a finite overlap between the quasiparticle and bare-electron operators. Moreover, the uncertainty principle implies the conjugate charge operator \hat{L}_τ experiences large fluctuations. Thus we can identify this phase with a Fermi liquid. On the other hand, when the charge operators \hat{L}_τ are pinned, which corresponds to small charge fluctuations, the conjugate phases are strongly fluctuating and $Z_\tau = 0$. This phase is thus associated with the Mott state.

Before applying the slave-rotor decomposition, however, it is essential to decompose the miniband dispersion, $\xi_{k\tau}$, Eq. (3), into two terms

$$\xi_{k\tau} = \bar{\epsilon}_\tau + \epsilon_{k\tau}, \quad (5)$$

where $\bar{\epsilon}_\tau$ is the average energy of the miniband ($\bar{\epsilon}_\tau = \sum_{k \in MBZ} \xi_{k,\tau}$), and the remainder, $\epsilon_{k\tau}$, is the kinetic part of the dispersion, which averages to zero. $\bar{\epsilon}_\tau$ can be interpreted as the effective binding energies of electrons to the respective minibands (dashed lines in Fig. 3). The importance of this decomposition is to separate these local energy shifts from the dispersion because they should not be renormalized by the quasiparticle weights Z_τ . Indeed, in the slave-rotor theory the quasiparticle weight only renormalizes the bandwidth but does not shift the average energy of the band [46].

Performing the slave-rotor decomposition to both species we obtain the Hamiltonian

$$\mathcal{H}_{SR} = - \sum_{ij\tau\sigma} (t_{ij}^{\tau\sigma} e^{i(\theta_{i\tau} - \theta_{j\tau})} + \delta_{ij} \bar{\epsilon}_\tau) f_{i\tau\sigma}^\dagger f_{j\tau\sigma} + \frac{U}{2} \sum_i (\hat{L}_{ia} + \eta \hat{L}_{ib})^2, \quad (6)$$

where $t_{ij}^{\tau\sigma}$ are the set of tight-binding parameters that reproduce the dispersive part ϵ_k in Eq. (3) when transformed to reciprocal space.

To assess the ground state of the Hamiltonian Eq. (6), we employ the variational method, as opposed to Ref. [46], where the self-consistent mean-field approach was used. Namely, we minimize the expectation value of Eq. (6) with respect to the variational wave function denoted by $|\Omega_V\rangle = |K_a, h_a\rangle \otimes |K_b, h_b\rangle \otimes |\mu_a\rangle \otimes |\mu_b\rangle$. This variational state is a product of the ground states of the rotor Hamiltonians,

$$H_\theta^\tau = \frac{1}{2} \hat{L}_\tau^2 + h_\tau \hat{L}_\tau + K_\tau \cos \theta_\tau, \quad (7)$$

and two Slater-determinant states (“Fermi sea” states) of the spinons, where the density is controlled by the chemical potentials μ_a and μ_b .

We must determine six variational parameters with three constraints ($\langle \hat{L}_\tau \rangle = \langle f_{i\tau}^\dagger f_{i\tau} \rangle - 1$ and $\sum_\tau \langle f_{i\tau}^\dagger f_{i\tau} \rangle = n$). The parameter K_τ controls whether species τ is metallic or localized. When the minimal energy solution is obtained with $K_\tau \neq 0$ the rotors are pinned and we get a finite quasiparticle weight $Z_\tau \neq 0$ corresponding to the metallic state. On the other hand, for $K_\tau = 0$ the rotors are in eigenstates of the angular momentum operator where the average of $e^{i\theta_\tau}$ vanishes, corresponding to the Mott state ($Z_\tau = 0$). Additionally, there is a freedom to redistribute charge between the two bands, which is controlled by the difference in the chemical potentials, $\mu_a - \mu_b$. Finally, the constraints are fulfilled using the three Lagrange multipliers h_τ and the sum $\mu_a + \mu_b$. Note that in the case of WS_2/WSe_2 , where the overlapping bands include one of the first excited bands of species a , which is more dispersive compared to the lowest band of species b , we apply the slave-rotor decomposition only to band b . For more details on the slave-rotor analysis we perform and the minimization procedure see Appendix C.

In Fig. 4 we plot the phase diagrams resulting from the variational minimization. Panels (a) and (d) correspond to the

WS_2/WSe_2 bilayer using $U = 60$ meV and $\eta = 1/2$. Figures 4(a) and 4(b) are maps of the filling of species b and a , respectively, in the space of total filling n and twist angle θ_M . In this case we recall that there is another completely filled miniband below the relevant pair of overlapping minibands [see Fig. 3(a)], and therefore the total filling is given by $n = 2 + n_a + n_b$. We turn our focus to the region inside the white dashed line, where the filling of species b is locked to unity while the filling of species a varies continuously [53]. In the same region we find that the quasiparticle weight Z_b vanishes [panel (d)]. Thus this region is identified as the OSM phase, where a lattice of localized magnetic moments coexists with itinerant electrons. Panel (c) shows the filling of each band for a specific twist angle $\theta_M = 3^\circ$, showing that the density of the itinerant band can be tuned over a large range inside the OSM phase.

In panels (e)–(h) in Fig. 4 we plot the results for $\text{MoS}_2/\text{MoSe}_2$ using $U = 40$ meV and $\eta = 1$. Panels (e) & (f) and (g) & (h) are maps of the filling and quasiparticle weight of species a and b , respectively. In Fig. 5 we plot the filling of each of the two bands vs total density for $\theta = 3.5^\circ$. We identify two OSM phases, one where band a is locked in a Mott state (marked OSM_a) and one where band b is locked in the Mott state (marked OSM_b). Additionally, at $n = 2$ there is a Mott state of both species, which is expected to have an approximate $\text{SU}(4)$ symmetry [54–57]. We also note that in this case, where the considered minibands are both the lowest of their corresponding species, there is no additional band filled in the background and the total density is given $n = n_a + n_b$.

For both materials, the OSM state assumes a large portion of the phase space (in Appendix C we show that this scenario is relevant to other TMD materials). For small twist angles, the density of itinerant electrons can be tuned between completely empty and completely filled states, which potentially allows one to tune the strength and sign of the RKKY interaction between local moments, which is mediated by the itinerant miniband [58]. At larger twist angles ($\theta_M \gtrsim 4^\circ$) the lattice of localized electrons melts into a Fermi liquid. Such a transition is characterized by the emergence of a Fermi surface which is not captured by the Ginzburg-Landau paradigm and is therefore of special interest [34,37,40,59].

We have also tested the stability of the OSM phase to variations in the parameters $\Delta\bar{\epsilon} = \bar{\epsilon}_a - \bar{\epsilon}_b$ and η numerically. In Appendix D we show that the range of filling where the OSM phase occurs is large for a wide range of $\Delta\bar{\epsilon}$ and η . We also roughly estimate this range analytically and find that it is expected to be large in the parameter regime $|\Delta\bar{\epsilon}| < U(1 - \eta)^2/2 - T_{it}$. Here $T_{it} < 0$ is the kinetic energy gain of filling the Fermi sea of the itinerant band minus the interaction energy associated with on-site fluctuations of charge. This analysis shows that the existence of a wide OSM phase is robust to the parameters of our model.

IV. EXPERIMENTAL CONSEQUENCES OF THE OSM STATE

We turn to discuss experimental consequences of the OSM phase. We first discuss the enlarged entropy associated with the formation of local moments. When the moments are free

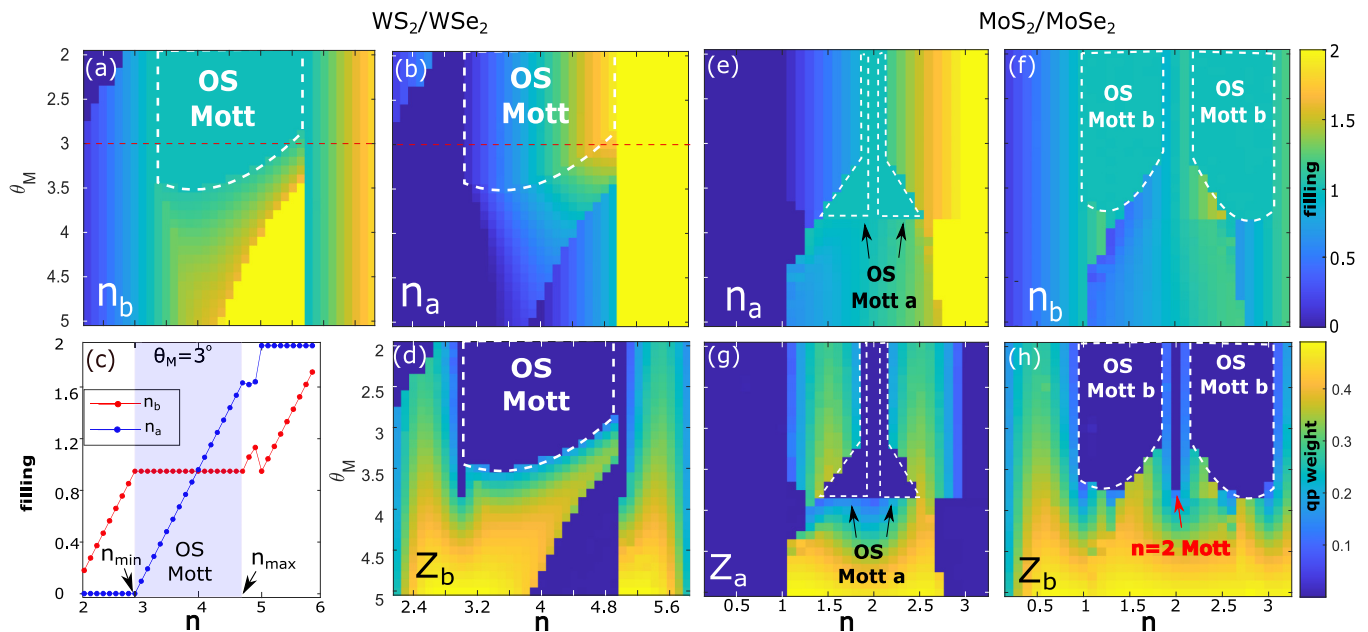


FIG. 4. Results of the slave-rotor mean-field theory. (a)–(d) Results for WS₂/WSe₂ at filling higher than 2 using $U = 60$ meV and $\eta = 1/2$. Note that the total filling ranges between 2 and 6 because there is one (lowest) miniband that is already filled and adds a background charge of 2. Thus each miniband (of *a* and *b*) accommodates only two electrons per moiré lattice site, one for each valley. (a) Color map of the density of band *b* in the space of filling *n* and twist angle θ_M . (b) The corresponding density map of band *a*. (d) Color map of the quasiparticle weight of species *b*. (c) The densities of species *a* and *b* at $\theta_M = 3^\circ$ vs total density. (e)–(h) Results for MoS₂/MoSe₂ using $U = 40$ meV and $\eta = 1$. (e, f) The density of species *a* and *b*, respectively. (g, h) Maps of the quasiparticle weights of species *a* and *b*, respectively. In all cases we observe finite regions, where the quasiparticle weight of a certain band falls to zero concomitant with odd integer filling. In these regimes the other species is in a compressible Fermi-liquid state and supports noninteger filling. These regimes thus realize the OSM and are marked by white dashed lines.

they contribute one k_B per lattice site. If a magnetic ordering is present, the local-moment contribution will be significant above the ordering temperature. Additionally, a distinct feature of this contribution will be a strong dependence on magnetic field. Indeed, the authors of Refs. [60,61] have recently measured such an enlarged entropy in twisted bilayer graphene (TBG), where they attributed it to local moments

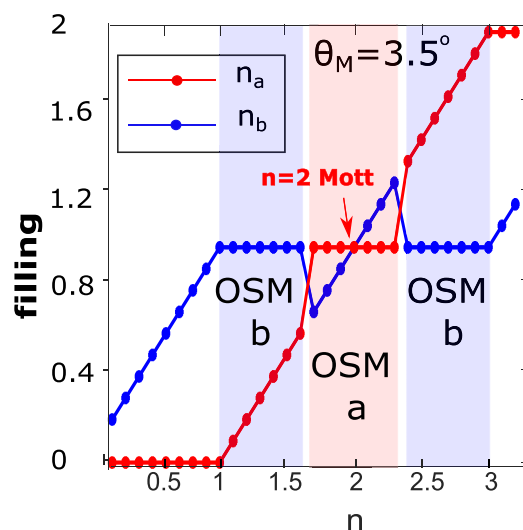


FIG. 5. The densities of species *a* and *b* at $\theta_M = 3.5^\circ$ vs total densities for MoS₂/MoSe₂ using $U = 40$ meV and $\eta = 1$.

coexisting with metallic states. Similarly, in the regime where both phases are metallic but close to the OSM regime we may expect a Pomeranchuk effect upon heating [60,61].

To estimate the change in entropy across the OSM transition, we assume the local moments contribute their maximal entropy, while the metallic states contribute $s_M = -\frac{2}{\Omega} \sum_{\tau, k \in BZ} [N_{k\tau} \log N_{k\tau} + (1 - N_{k\tau}) \log(1 - N_{k\tau})]$, where $N_{k\tau}$ are the momentum space Fermi-Dirac distribution functions, which include the effects of the quasiparticle weight Z_τ . In Fig. 6 we plot the entropy per moiré lattice site as a function of density for the WS₂/WSe₂ bilayer at $\theta_M = 2.5^\circ$ for three different temperatures. The distinct signature is a large jump at the boundaries of the OSM state, where we also observe an enhanced specific heat manifested in the strong dependence of S with T .

Another suitable probe for the OSM state is magneto-transport [40], especially given that we predict this state at a relatively high density range $n \sim 2-4$, where the effects of disorder are less prominent as compared with the filling range of the lowest miniband. Inside the OSM phase the Hall number, which is seen both in the slope of the classical Hall resistivity and in the period of quantum oscillations, will correspond to a “small” Fermi surface (of volume $n_b = n - 1$). At the phase transition point [green hue in Fig. 1(c)] the local moments melt into a metallic state, manifested in a Lifshitz transition, where we can distinguish two scenarios. When the dominant exchange interaction between the two species is antiferromagnetic we expect a heavy-Fermi-liquid state to emerge between the fully metallic phase and the magnetic

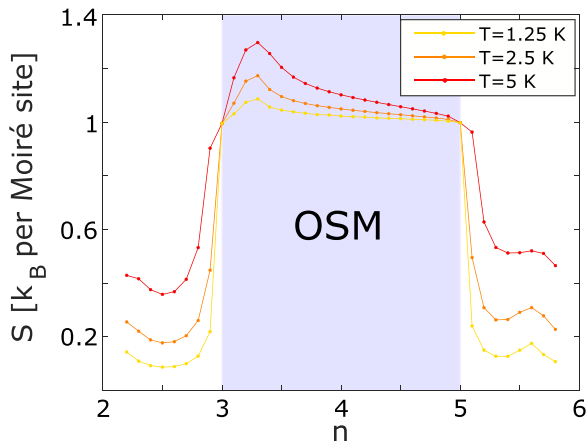


FIG. 6. The entropy per site in units of $k_B \log 2$ as a function of filling at angle $\theta_M = 2.5^\circ$ for three different temperatures. Here the Mott state is assumed to contribute one bit per site.

metal. In this case the Hall number changes from the “small” volume $n - 1$ to the “large” volume n . The second scenario is where the exchange interaction is dominated by ferromagnetic exchange (e.g., due to the orbital Hund’s coupling). In this case theory does not predict the emergence of a hybridization gap between the local and itinerant electrons. Instead, a new Fermi surface emerges at the transition point. Thus we expect the appearance of beating in quantum oscillations and nonlinearity of the classical Hall effect (see, for example, Ref. [62]). Thus magnetotransport measurements across the melting transition can also distinguish the nature of the magnetic exchange mechanism.

Finally, another prominent feature of the OSM phase can be seen in the dependence of the compressibility on density. As can be seen in Fig. 5, inside the OSM phase and close to the transition the itinerant band develops negative compressibility $\partial n / \partial \mu < 0$ [63,64]. This is because the incompressible state forms before half filling on the expense of the itinerant electron band. As a consequence, the density of the compressible band drops near the transition.

V. SUMMARY

We proposed that electron-doped TMDs subject to a moiré potential are prime candidates to realize the Kondo lattice model. The essential ingredient is the multiplicity of electron band minima close to the K and K' points, which allows for two moiré bands of different widths to be simultaneously at partial filling. We used a simplified model with constant on-site Coulomb repulsion and a slave-rotor mean-field theory to study the possible ground states of the system. We found a large phase space, where an orbitally selective Mott phase forms. Such a state is characterized by a Mott state of one species coexisting with a metallic state of the other. This opens a path to simulate the Kondo lattice model and possible exotic phase transitions in TMD moiré devices.

Note added. Upon completion of this paper we came to learn about a related theoretical proposal regarding trilayers of twisted graphene sheets [65].

ACKNOWLEDGMENTS

We are grateful to Erez Berg, Debanjan Chowdhury, Rafael Fernandes, Efrat Shimshoni, Inti Sodemann, and Arun Parameknti for helpful discussions. This research was funded by the Israeli Science Foundation under Grant No. 994/19. J.R. acknowledges the support of the Alon Fellowship awarded by the Israel Higher Education Council.

APPENDIX A: CONTINUUM DISPERSION

In this Appendix we provide additional information about the computation of the continuum Hamiltonian. We start with the tight-binding approximation for single-layer semiconducting TMDs of the trigonal prismatic structure (H) [44]. This model consists of three orbitals d_{z^2} , d_{xy} , and $d_{x^2-y^2}$, taking into account spin-orbit coupling and hopping up to the third nearest neighbors on the triangular lattice. The conduction band consists of two Bloch bands denoted by $\tau = a, b$, which are plotted in Fig. 2 (colored red and blue, respectively) and will be referred to as “species” henceforth. Each such band has two parabolic minima near the K and K' , corresponding to spin states $\sigma = \uparrow \downarrow$. (The valley and spin are locked; however, it is important to note that the spin orientations near K and K' are opposite in the two Bloch bands.) Up to quadratic order in deviations from the high-symmetry points we obtain the Hamiltonian

$$\hat{H}_0 = \sum_{k\tau\sigma} c_{k\tau\sigma}^\dagger \left(\Delta_\tau + \frac{k^2}{2m_\tau} \right) c_{k\tau\sigma}. \quad (\text{A1})$$

Here Δ_τ and m_τ are species-dependent band minimum and mass, respectively. \mathbf{k} is the lattice momentum relative to the high-symmetry points, i.e., relative to \mathbf{K} for (a, \uparrow) , (b, \downarrow) and relative to \mathbf{K}' for (b, \uparrow) , (a, \downarrow) . A crucial feature that is unique to the conduction bands, is that the higher-order spin-orbit splitting, $|\Delta_a - \Delta_b|$, is comparable to the expected moiré lattice depth and resulting miniband width (see Table I).

We now turn to consider the effect of a moiré potential, which we assume is induced by a second layer. At small twist angles $\theta_M \ll \pi$ the superlattice constant is given by $a_M \approx a/\theta_M$, where $\theta_M \equiv \sqrt{\delta^2 + \theta^2}$, δ is the mismatch between the layers taken from Ref. [20], and θ accounts for any additional twist. In this limit we have $a_M \gg a$, which justifies the use of a simple triangular periodic potential constructed out of the six smallest harmonics $G_j = \hat{R}(j\frac{\pi}{3})(4\pi/\sqrt{3}a_M\hat{x})$, $j = 0, \dots, 5$:

$$V_M(r) = \sum_i V_0(G_i) e^{-iG_i \cdot r}. \quad (\text{A2})$$

The potential has threefold rotational symmetry which states that $V_0[\hat{R}(\frac{2}{3}\pi)G_i] = V_0(G_i)$ and $V_0(-G_i) = V_0^*(G_i)$. To obtain the miniband structure of the lowest minibands, we use a 19-band model without counting degeneracy of spin and species. For simplicity we take the moiré potential strength to be uniform across platforms and given by $V_0 = 15$ meV [19,20].

In Fig. 3 we compare the two lowest minibands for the two species (species a colored blue, and species b colored red) for realistic parameters of two candidate materials. As can be seen, a feature of these miniband structures is the overlap of bands belonging to different species. Note that the overlapping minibands are not necessarily the same numeral subband.

As shown in panel (a) for WS_2 , the overlap is between the first excited band of one species and the lowest miniband of the other (the same is true for WSe_2 and MoSe_2). On the other hand, for MoS_2 the overlap occurs between the lowest minibands of the two species [panel (b)]. Upon restriction to the two bands of interest (namely, those that are overlapping), we obtain the dispersion in Eq. (3).

APPENDIX B: INTERACTIONS

In the paper we assume a contact interaction of the form

$$\mathcal{H}_I = \frac{1}{2} \sum_{i\tau\tau'} U_{\tau\tau'} \delta n_{i\tau} \delta n_{i\tau'}, \quad (\text{B1})$$

where $\delta n_{i\tau} = \psi_{i\tau}^\dagger \psi_{i\tau} - 1$. Notice that we have written the interaction in a particle-hole symmetric manner, which can be absorbed into the parameters $\bar{\epsilon}_\tau$ in Eq. (5).

The relative strength of the interaction parameters $U_{\tau\tau'}$ depend on the spread of the Wannier orbitals of the corresponding minibands [19,20]. Namely, when both minibands are the lowest subband of their corresponding species [as shown for MoS_2 in Fig. 3(b)], the spread of the two Wannier functions is approximately the same, and we expect $U_{aa} \simeq U_{ab} \simeq U_{bb}$. In this case the interaction (B1) is proportional to the square of total density.

On the other hand, when the two overlapping bands belong to different subbands [see WS_2 , in Fig. 3(a)], their corresponding Wannier functions will differ in width (namely, the higher, more dispersive band will have a larger spread). Thus in this case, the interaction parameters may differ significantly. To account for this effect we consider the phenomenological parameter η such that $U_{bb} = \eta U_{ab} = \eta^2 U_{aa}$. The interaction equation (B1) then assumes the form

$$\mathcal{H}_I = \frac{U}{2} \sum_i (\eta \delta n_{ia} + \delta n_{ib})^2, \quad (\text{B2})$$

where $\eta < 1$ describes the scenario where the Wannier function of band b has a smaller spread when compared to a .

The value of U itself is twist-angle dependent [19]. For simplicity, however, we will take a constant value $U = 60$ meV for WS_2 , WSe_2 , and MoSe_2 , which corresponds to a dielectric environment of $\epsilon = 5$ [51]. For MoS_2 we use $U = 40$ meV. We note these values are weaker than those used in other studies estimates [20,66].

The quadratic form of the interaction (B2) was chosen for simplicity. In general, the ratio between the inter- and intraspecies interactions is not controlled by a single parameter η . Therefore, it is important to note that the OSM phase space is expected to be reduced in the case where the interspecies interaction U_{ab} becomes much larger than U_{aa} or U_{bb} . As we show in Appendix D and in the analysis of MoS_2 with $\eta = 1$, however, the OSM state is not very sensitive to large interspecies interaction. Another crucial interaction we have neglected is longer-range interaction. We expect these interactions to cause additional Wigner crystal insulating phases to appear. They will likely cause the phase space of the OSM state to shrink as well. However, these incompressible states may also stabilize over a finite range of doping with the aid of a background incompressible state, i.e., forming an orbitally

selective Wigner crystal. Finally, we have also neglected spin-exchange interactions (e.g., Hund's), which will be discussed in Appendix E.

APPENDIX C: DETAILS OF THE VARIATIONAL MINIMIZATION OF THE SLAVE-ROTOR MEAN-FIELD FREE ENERGY

In this section we describe in more detail the slave-rotor mean-field theory [46–48] that we have used in the main text. We first decompose the field operators into bosonic rotors ($e^{-i\theta_{i\tau}}$) multiplied by neutral spinon operators ($f_{i\tau}$):

$$\psi_{i\tau\sigma} = e^{-i\theta_{i\tau}} f_{i\tau\sigma}. \quad (\text{C1})$$

The respective density operator of each species, which are conjugates of the phases above, are then written in terms of angular momentum operators

$$\hat{L}_{i\tau} = -i \frac{\partial}{\partial \theta_{i\tau}} \quad (\text{C2})$$

subject to the *local* constraint

$$\hat{L}_{i\tau} = f_{i\tau}^\dagger f_{i\tau} - 1,$$

where the sum over spin is implicit. The application of the slave-rotor decomposition to Eqs. (3) and (4) of the main text enables a simple mean-field analysis, which captures the localization-delocalization transition of a half-filled band.

This decomposition allows for a mean-field treatment of the Mott transition. The “order parameter” is the quasiparticle weight $Z_\tau = |\langle e^{i\theta_\tau} \rangle|^2$. When the rotor's phase θ_τ assumes a finite expectation value, $Z_\tau \neq 0$ and the spinon quasiparticles have a finite overlap with the original electronic operator. This phase thus corresponds to a Fermi-liquid state. On the other hand, when θ is delocalized the rotor $e^{i\theta_\tau}$ has a vanishing expectation value and the quasiparticle weight disappears ($Z_\tau = 0$), corresponding to a Mott phase.

Below we will describe two approaches. First, we will consider the case where only one species is decomposed (the flatter of the two). This case is more applicable to a situation where the density of states of the two bands differs significantly. In the second case we will consider the same analysis where both bands are decomposed.

1. Slave-rotor decomposition of a single band in a two-band system

Applying the aforementioned slave-rotor decomposition to the flatter band (for the purpose of the discussion let it be $\tau = b$), as is the case for Eqs. (3) and (4), we obtain

$$\begin{aligned} \mathcal{H}_{SR} = & - \sum_{ij} (t_b^{ij} e^{i(\theta_{ib} - \theta_{jb})} f_{ib}^\dagger f_{jb} + t_a^{ij} \psi_{ia}^\dagger \psi_{ja}) \\ & + \sum_i (\bar{\epsilon}_b f_{ib}^\dagger f_{ib} + \bar{\epsilon}_a \psi_{ia}^\dagger \psi_{ia}) + \frac{U}{2} \sum_i (\hat{L}_{ib} + \eta \delta n_{ia})^2, \end{aligned} \quad (\text{C3})$$

where t_τ^{ij} are the set of tight-binding parameters that reproduce the dispersive part ϵ_k in Eq. (5) when transformed to reciprocal space.

To estimate the location of possible Mott phases of Eq. (C3) we use a variational approach. This should be

contrasted with Ref. [46], where the self-consistent mean-field technique was used. In the variational approach we minimize the expectation value of Eq. (C3) with respect to a variational wave function denoted by $|\Omega_V\rangle = |K_b, h_b\rangle \otimes |\mu_b\rangle \otimes |\mu_a\rangle$, which is a product of the ground states of the following variational Hamiltonians:

$$H_\theta^b = \frac{1}{2} \hat{L}_b^2 + h_b \hat{L}_b + K_b \cos \theta_b, \quad (\text{C4})$$

$$H_f^b = \sum_k (\epsilon_{kb} - \mu_b) f_{kb}^\dagger f_{kb}, \quad (\text{C5})$$

$$H_\psi^a = \sum_k (\epsilon_{ka} + \Delta\bar{\epsilon} - \mu_a) \psi_{ka}^\dagger \psi_{ka}, \quad (\text{C6})$$

where we have shifted the energies such that the center of band b is at zero and $\Delta\bar{\epsilon} = \bar{\epsilon}_a - \bar{\epsilon}_b$. Equation (C4) controls the rotor field, where the term proportional to K_b acts to pin the phase θ_b , giving rise to a finite quasiparticle weight Z_b . Thus we can identify the Fermi-liquid (Mott) phases with situations where the minimal energy solution is obtained with $K_b \neq 0$ ($K_b = 0$). The parameter h_b is used to obey the slave-rotor constraint on average. The second and third variational Hamiltonians Eqs. (C5) and (C6) generate Fermi sea states of spinons and a electrons, with density controlled by the parameter μ_b and μ_a , respectively. Notice that the ground state of Eq. (C5) is independent of the bandwidth and therefore Z_b is omitted.

We then minimize the expectation value of the full Hamiltonian Eq. (6), denoted by

$$F(K_b, h_b, \mu_b, \mu_a) = \langle \Omega_V | \mathcal{H}_{SR} | \Omega_V \rangle,$$

with respect to the four parameters K_b , h_b , and μ_b and μ_a subject to two constraints:

$$\langle \hat{L}_b \rangle = \langle f_{ib}^\dagger f_{ib} \rangle - 1 \quad \langle f_{ib}^\dagger f_{ib} \rangle + \langle \psi_{ia}^\dagger \psi_{ia} \rangle = n. \quad (\text{C7})$$

The difference between the number of constraints and variational parameters implies that two are free. These correspond to the quasiparticle weight of band b and any distribution of the total density between the bands. These two parameters are dictated by energetics.

Notice that in using Eq. (7) we have neglected spatial fluctuations of the field θ_b . This restricts our ground-state manifold (for example, it cannot capture spin correlations [47]). However, it allows for a significant simplification: The expectation value of the rotor correlation function becomes a product of local expectation values $\langle e^{i(\theta_{it} - \theta_{j\tau})} \rangle = \langle e^{i\theta_{it}} \rangle \langle e^{-i\theta_{j\tau}} \rangle = Z_\tau$. Consequently, the expectation value of the kinetic energy terms can be straightforwardly transformed back to momentum space, reproducing the exact continuum dispersion relation, Eq. (3):

$$F = \sum_k [Z_b \epsilon_{kb} N_{kb} + (\epsilon_{ka} + \Delta\bar{\epsilon}) N_{ka}] + \frac{U}{2} \sum_i [(L_b^2) + 2\eta(L_b)(n_a - 1) + \eta^2((n_a - 1)^2)], \quad (\text{C8})$$

where $N_{kb} = N_0(\epsilon_{kb} - \mu_b)$, $N_{ka} = N_0(\epsilon_{ka} + \Delta\bar{\epsilon} - \mu_a)$, and $N_0(x) = 1/(e^{\beta x} + 1)$. Here β is the inverse temperature, which will be taken to infinity $\beta \rightarrow \infty$, which is used as a numerical parameter to smooth the discretization.

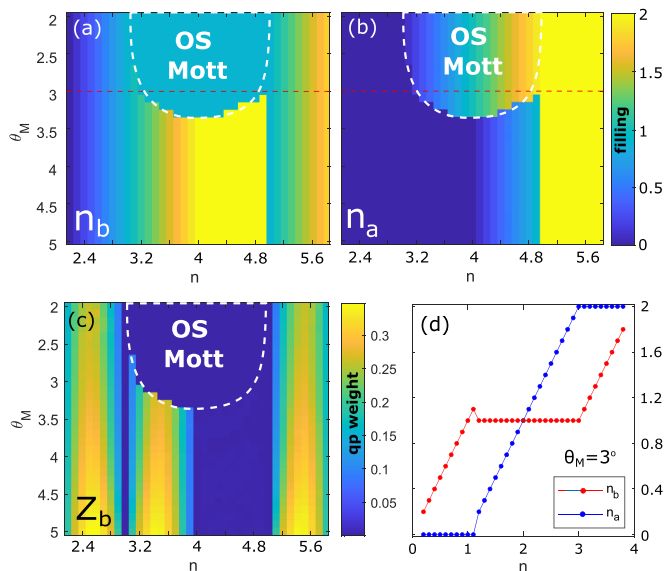


FIG. 7. The results of the slave-rotor mean-field analysis for MoSe₂, $U = 60$ meV, and $\eta = 1/2$. (a, b) The density of the two species in the space of the moiré angle θ_M and total density n . (c) Quasiparticle weight of species b , Z_b . The region of half filling $n_b = 1$ and $Z_b = 0$ corresponds to a Mott state of band b . (d) The densities of bands a and b at θ_M vs total density.

In panels (a)–(d) of Figs. 4, 7, and 8 we plot the phase diagram obtained from minimizing Eq. (C8) for the band-structure parameters of WS₂, MoSe₂, and WSe₂, respectively. Note that as opposed to the main text, we do not specify the precise bilayer composition. For each TMD material here, one must consider a second “inactive” layer that induces the moiré

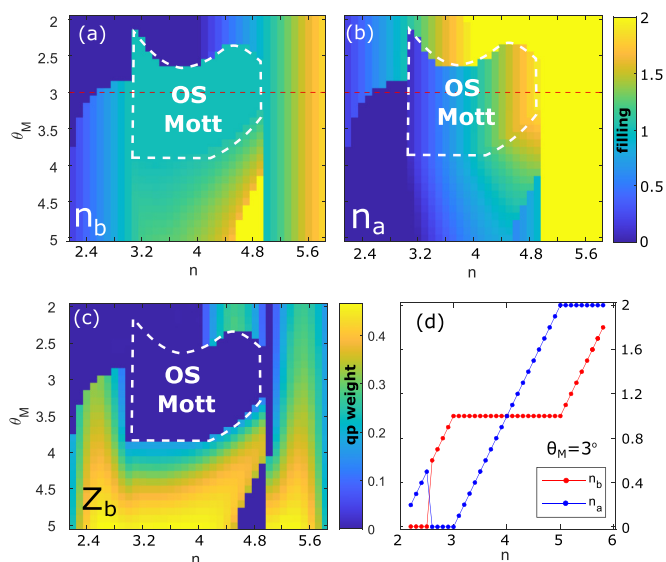


FIG. 8. The results of the slave-rotor mean-field analysis for WSe₂, $U = 60$ meV, and $\eta = 1/2$. (a, b) The density of the two species in the space of the moiré angle θ_M and total density n . (c) The quasiparticle weight of species b , Z_b . The region of half filling $n_b = 1$ and $Z_b = 0$ corresponds to a Mott state of band b . (d) The densities of bands a and b at θ_M vs total density.

potential and has band alignment properties that ensure it has a higher-in-energy conduction band. We use $U = 60$ meV and $\eta = 1/2$. Panels (a) and (b) are maps of the density of bands b and a , respectively, in the space of total density n and twist angle θ_M . Panel (c) is the corresponding quasiparticle weight Z_b . Panel (d) shows the relative filling at $\theta_M = 3$. There are two distinct regimes as a function of angle. For $\theta_M < 3.5$, the filling of band b is roughly split in half. Between $n = 0$ and $n = 1$, band b fills until it reaches a localized state (characterized by $Z = 0$ and $n_b = 1$). Then band b fills continuously between $n = 1-3$. Finally, band b continues to fill until $n = 4$ is reached. The regime where band a is continuously filling realizes an orbitally selective Mott phase, where a Kondo lattice model is expected to be simulated with variable itinerant electron density.

On the other hand, for $\theta_M > 3.5$ the bands fill up one-by-one. In particular, band b fills completely between $n = 2$ and $n = 4$ with a Mott state at $n = 5$. Then above $n = 5$ it resets back into the Mott state and band a fills completely. This behavior thus, resembles a Stoner-like polarization of the species. However, we comment that the slave-rotor mean field tends to overestimate the size of band-polarized regions. This is because it overestimate the contribution of charge fluctuations to the interaction energy when the filling differs significantly from $1/2$.

2. Two-band slave-rotor decomposition

As explained in the case of MoS₂, the electronic bands experience a much weaker spin-orbit coupling. Consequently, the shape and effective binding energies are almost identical [see Table I and Fig. 3(b)]. In this case it makes sense to decompose both bands in an unbiased manner,

$$\begin{aligned} \mathcal{H}_{SR} = & - \sum_{ij\tau} t_{ij}^{ij} e^{i(\theta_{i\tau} - \theta_{j\tau})} f_{i\tau}^\dagger f_{j\tau} \\ & - \sum_{i\tau} \bar{\epsilon}_\tau f_{i\tau}^\dagger f_{i\tau} + \frac{U}{2} \sum_i (L_{ia} + L_{ib})^2, \end{aligned} \quad (\text{C9})$$

where $\eta = 1$ and $\Delta\bar{\epsilon} = \bar{\epsilon}_a - \bar{\epsilon}_b$ is much smaller than the bandwidth and U .

Following the previous section, we now use four variational Hamiltonians of the form of Eqs. (7) and (C5), which generate a ground state $|K_\tau, h_\tau, \mu_\tau\rangle$ controlled by six variational parameters and subject to three constraints:

$$\langle \hat{L}_\tau \rangle = \langle f_{i\tau}^\dagger f_{i\tau} \rangle - 1 \quad ; \quad \langle f_{ia}^\dagger f_{ia} \rangle + \langle \varphi_{ib}^\dagger \varphi_{ib} \rangle = n. \quad (\text{C10})$$

In panels (e)–(h) of Fig. 4 of the main text we plot the phase diagram resulting from the minimization of the expectation value of Eq. [9] As can be seen, at $n = 2$ both Z_a and Z_b equal zero for small enough angles. The similarity of the bands of the two species leads us to propose electron-doped MoS₂ as a candidate material to realize an SU(4) symmetric Mott insulator on a triangular lattice, which is an interesting problem in its own right [54,55].

3. Details of the numerical minimization procedure

In this Appendix we provide the details of the numerical minimization procedure of Eq. (C8). To calculate this

functional, we performed straightforward Brillouin zone integration on a square grid of size 150×150 . The integration itself was performed by MATLAB's *trapezoidal* numerical integration, and the Fermi-Dirac distribution was written as $N_0(\epsilon_k) = \frac{1}{1+e^{-\beta\epsilon_k}}$, with $\beta = \frac{1}{T}$ being the inverse temperature. To broaden the discretization we use a finite temperature $\beta = 60/\max(\epsilon_a)$. In addition, the minimal ground state that was found for the phase diagram in Fig. 3 was found by MATLAB's minimization algorithm *fmincon*, which minimizes the functional Eq. (C8), under the constrains of Eq. (C7) by means of the specified variational parameters. The optimization algorithm that was found to converge most efficiently was the *interior-point* algorithm, which is the default algorithm of *fmincon*.

APPENDIX D: ON THE STABILITY OF THE OSM STATE TO VARIATIONS OF PHENOMENOLOGICAL PARAMETERS

In the main text we have presented the results of a slave-rotor mean-field analysis, where bands of different species fill either one-by-one or simultaneously, depending on the twist angle. The latter scenario is of particular interest to us, as it gives way to the orbitally selective Mott phase.

Given that we have a number of unknown parameters, including η and the energy difference

$$\Delta\bar{\epsilon} = \bar{\epsilon}_a - \bar{\epsilon}_b, \quad (\text{D1})$$

it is important to test the stability of the OSM state. In this Appendix we compute a lower bound on the phase-space volume of the OSM state in the space of $\Delta\bar{\epsilon}$ and η .

To obtain this estimate we focus specifically on the commensurate filling $n = 2$ (or $n = 4$ for the strongly spin-orbit-coupled bilayer WS₂/WSe₂). If the bands fill one-by-one, this filling point will be characterized by one completely filled band and another completely empty. On the other hand, if the bands fill simultaneously, this filling value is likely to be characterized by a partial filling of both bands with total density of unity. Here we will make a restrictive assumption that both bands are at filling unity, where one is in a Mott state and the other is either metallic or also in a Mott state. The phase diagrams we have computed are consistent with this behavior at filling $n = 2$ (or 4).

Under this assumption we can estimate the expectation value of the Hamiltonian Eq. (6) within these restrictive trial states:

$$\begin{aligned} |F_a\rangle &= |n_a = 2\rangle \otimes |n_b = 0\rangle, \\ |F_b\rangle &= |n_a = 0\rangle \otimes |n_b = 2\rangle, \\ |P\rangle &= |n_a = 1\rangle \otimes |n_b = 1\rangle, \end{aligned} \quad (\text{D2})$$

and compare which of them has a lower energy. The first two states represent fully polarized states and thus correspond to the scenario where the band fills one-by-one. The third state, however, is where the filling is shared between the two bands. We will further assume that band a is the flatter of the two bands and is in a Mott state at $n_a = 1$. The energy per unit cell

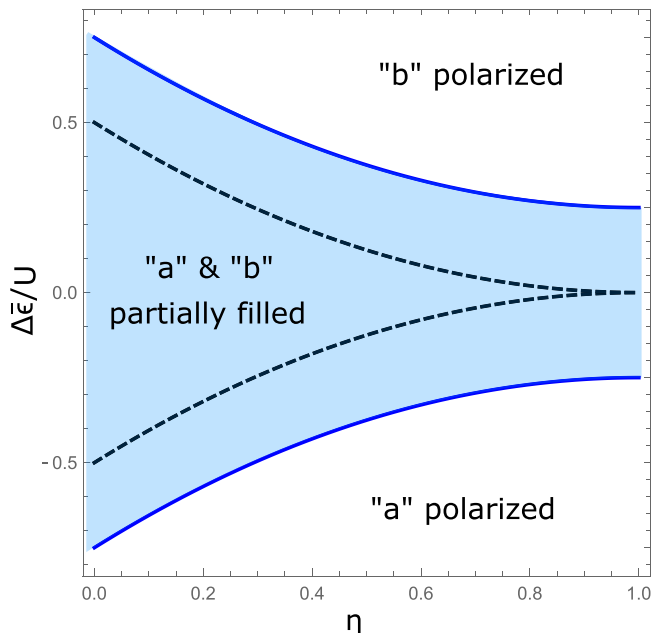


FIG. 9. Stability of simultaneous occupation of two moiré mini-bands for filling $n = 2$ (or $n = 4$ for the strongly spin-orbit-coupled bilayer WS_2/WSe_2) in the space of $\Delta\bar{\epsilon}$ and the phenomenological parameter η . The blue lines correspond to $T_{\text{it}} = -U/4$ (species b in a metallic state), and the dashed lines are the case $T_{\text{it}} = 0$ (species b also in a Mott state).

of these three states is given by

$$\begin{aligned} E_a &\equiv \frac{\langle F_a | \mathcal{H}_{\text{SR}} | F_a \rangle}{\Omega} = 2\bar{\epsilon}_a + \frac{U}{2}(1 - \eta)^2, \\ E_b &\equiv \frac{\langle F_b | \mathcal{H}_{\text{SR}} | F_b \rangle}{\Omega} = 2\bar{\epsilon}_b + \frac{U}{2}(1 - \eta)^2, \\ E_{ab} &\equiv \frac{\langle P | \mathcal{H}_{\text{SR}} | P \rangle}{\Omega} = \bar{\epsilon}_a + \bar{\epsilon}_b + T_{\text{it}}. \end{aligned} \quad (\text{D3})$$

Here Ω is the total number of sites. $T_{\text{it}} \leq 0$ is the sum of the negative kinetic energy associated with half-filling band b , and the interaction energy associated with the charge fluctuations $\Delta n_b^2 = \langle (n_b - 1)^2 \rangle$ at the half-filling point. Thus, when $T_{\text{it}} < 0$ band b remains in a metallic state and reaches zero when it falls into a Mott state as well.

When $E_{ab} < \min(E_a, E_b)$ the third state (simultaneous filling) is more favorable energetically. On the other hand, when E_a or E_b are minimal, the ground state can be band polarized (but not necessarily), where the bands fill one-by-one.

Comparing these energies, we conclude that the partial filling state is stable at least in the regime

$$|\Delta\bar{\epsilon}| < U(1 - \eta)^2/2 - T_{\text{it}}. \quad (\text{D4})$$

In Fig. 9 we plot the stability region defined by Eq. (D4) for the case of $T_{\text{it}} = -U/4$. The case of $T_{\text{it}} = 0$ is also plotted for comparison (dashed line).

Given that $T_{\text{it}} \leq 0$, there exists such a regime for any value of η . Note that the width in $\Delta\bar{\epsilon}$ of this window scales with U at strong coupling. We thus conclude that the regime of partial occupation of both bands is wide and robust to parameters

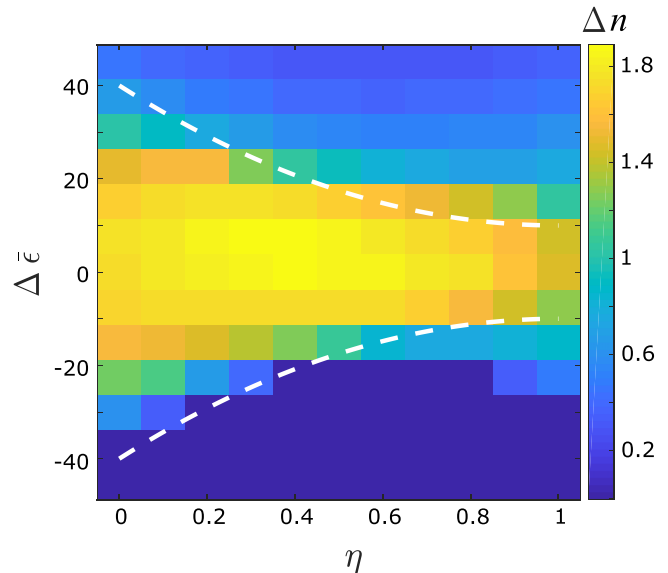


FIG. 10. Stability diagram of the coexistence of localized and itinerant states in the space of η and $\Delta\bar{\epsilon}$ with $U = 60$ meV obtained from numerical minimization of Eq. (C8). The color bar denotes the width of the Mott region in filling averaged over all angles between 2° and 5° (the maximal width is 2). The white dashed line is the analytic estimate, where the two species are expected to be simultaneously at partial filling at $n = 4$, Eq. (D4), with $T_b = -10$ meV.

such as the ratio of species interaction η and splitting of the bands $\Delta\bar{\epsilon}$.

In Fig. 10 we plot the width of the OSM phase $\Delta n = n_{\text{max}} - n_{\text{min}}$ averaged over the angles 2° and 5° , which is obtained from the numerical minimization of Eq. (C8). Here n_{max} and n_{min} mark the boundaries of the OSM phase per angle (maximal value is 2), as shown in Fig. 4(c). The white dashed line is the analytic estimate Eq. (D4). We thus, conclude that the OSM phase is not sensitive to parameters and is a generic feature of the phase diagram of electron-doped moiré TMDs.

APPENDIX E: SPIN-EXCHANGE INTERACTIONS AND EXPECTED PHENOMENOLOGY

Inside the OSM, phase charge fluctuations of the localized species are quenched and therefore the relevant interspecies interactions are of spin-exchange type. In this section we discuss two such interactions and their possible influence on the magnetic ground state.

We anticipate that the ferromagnetic Hund's coupling is the largest exchange mechanism,

$$\mathcal{H}_H = - \sum_i J_H (\psi_{i\uparrow}^\dagger \sigma \psi_{i\downarrow}) \cdot \mathbf{S}_i, \quad (\text{E1})$$

where \mathbf{S}_i is the spin of the localized moments at site i (let us assume they belong to species a). Using standard harmonic oscillator states, we estimate $J_H \approx 0.2U$.

Upon approaching the melting point of the OSM state, however, other interaction terms compete with Eq. (E1), for example, the interaction that scatters across the original Brillouin zone. To see this let us first write this term in terms of the original operators Eq. (1),

$\mathcal{H}_J = J_P \sum_{k,k',p} c_{k+pa\uparrow}^\dagger c_{k'-pa\downarrow}^\dagger c_{k'b\downarrow} c_{kb\uparrow} + \text{H.c.}$, where $J_P/U \sim a/a_M \approx \sqrt{\delta^2 + \theta_M^2}$ (for an angle of $\theta_M = 3.5^\circ$ we obtain $J_P \approx 0.1U$). Taking into account the moiré potential and the slave-rotor decomposition described above, this interaction assumes the form

$$\mathcal{H}_J = \tilde{J}_P \sum_{k,k',p} f_{k+pa\uparrow}^\dagger f_{k'-pa\downarrow}^\dagger \psi_{k'b\downarrow} \psi_{kb\uparrow} + \text{H.c.}, \quad (\text{E2})$$

where $\tilde{J}_P = Z_a J$. Thus when the band a is localized and $Z_a = 0$ this term vanishes. However, if the local moments are incorporated into the Fermi surface (through the formation of a heavy-Fermi liquid) they reacquire a finite quasiparticle weight Z [48]. Thus this interaction can become important close to the melting point of the local-moment lattice.

As mentioned above, inside the OSM phase we expect the dominant exchange to be Hund's and therefore spin correlations to be ferromagnetic, as in Ref. [29]. When the Hund's coupling Eq. (E1) is dominant, the main influence of the itinerant electrons inside the OSM state is to mediate long-range RKKY interactions [58],

$$\mathcal{H}_{\text{RKKY}} \approx \frac{J_H^2 \nu_0 k_F^2}{8\pi} \sum_{ij} \frac{\sin k_F R_{ij}}{R_{ij}^2} \mathbf{S}_i \cdot \mathbf{S}_j, \quad (\text{E3})$$

where ν_0 is the density of states. Thus, as the filling of the itinerant band is modified from zero to 2, the *nearest-neighbor* interaction mediated by the electrons can be tuned from ferromagnetic in the dilute limit to antiferromagnetic and back to ferromagnetic (going through a van Hove singularity). This interaction is added to the direct superexchange between sites [19], which may have a cooperative effect or frustrate the magnetic interactions.

APPENDIX F: THE HEAVY-FERMI-LIQUID STATE

When the antiferromagnetic correlations dominate we expect a heavy-Fermi-liquid state to compete with the internal magnetic interactions. For completeness, in this Appendix we compute the Kondo temperature assuming $\tilde{J}_P = 4$ meV

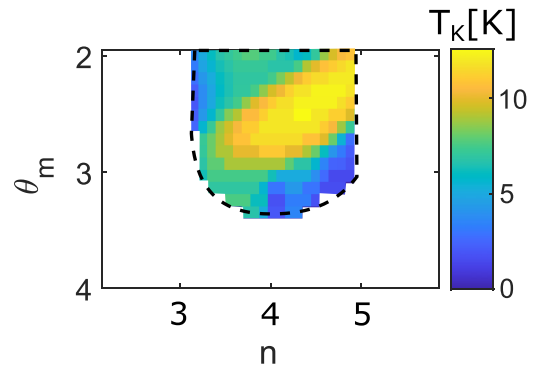


FIG. 11. The Kondo temperature inside the OSM state for MoSe₂.

within the large- N mean-field theory [67]. We find that $T_K \sim 5\text{--}15$ K inside the OSM phase and therefore, we expect that if the antiferromagnetic correlations dominate the OSM melting transition can be accompanied by a detectable heavy-Fermi-liquid state. Moreover, in this case the tunability of the itinerant electron density may allow tuning through the Doniach phase diagram [25].

Let us briefly describe the large- N mean-field theory. The dispersion of the two species is taken to be

$$\mathcal{H}_{MF} = \sum_k [(Z_b \epsilon_{kb} - \mu_b) f_{kb}^\dagger f_{kb} + (\epsilon_{ka} - \Delta \bar{\epsilon} - \mu_a) \psi_{ka}^\dagger \psi_{ka}], \quad (\text{F1})$$

where the density of each species n_τ is set separately using the Lagrange multipliers μ_τ according to their values in the slave-rotor mean-field calculation. We then decouple Eq. (E2) using the mean-field hybridization $\chi = J/2 \langle f_{b\sigma}^\dagger \psi_{a\sigma} \rangle + \text{c.c.}$. We then solve for χ self-consistently, while tuning μ_a and μ_b to conserve the density of a and b on average. The Kondo temperature is then estimated by seeking the lowest temperature where there is a self-consistent solution for $\chi = 0$. To obtain the Kondo temperature T_K we estimate the lowest temperature where $\chi = 0$.

In Fig. 11 we plot the resulting Kondo temperature as a function of twist angle and density for $\tilde{J} = 4$ meV. As can be seen, the Kondo temperature is measurable in standard cryosthetics and might be physically important.

-
- [1] R. Bistritzer and A. H. MacDonald, Moiré bands in twisted double-layer graphene, *Proc. Natl. Acad. Sci. USA* **108**, 12233 (2011).
- [2] Y. Cao, V. Fatemi, S. Fang, K. Watanabe, T. Taniguchi, E. Kaxiras, and P. Jarillo-Herrero, Unconventional superconductivity in magic-angle graphene superlattices, *Nature (London)* **556**, 43 (2018).
- [3] M. Yankowitz, S. Chen, H. Polshyn, Y. Zhang, K. Watanabe, T. Taniguchi, D. Graf, A. F. Young, and C. R. Dean, Tuning superconductivity in twisted bilayer graphene, *Science* **363**, 1059 (2019).
- [4] X. Lu, P. Stepanov, W. Yang, M. Xie, M. A. Aamir, I. Das, C. Urgell, K. Watanabe, T. Taniguchi, G. Zhang *et al.*, Superconductors, orbital magnets and correlated states in magic-angle bilayer graphene, *Nature (London)* **574**, 653 (2019).
- [5] L. Balents, C. R. Dean, D. K. Efetov, and A. F. Young, Superconductivity and strong correlations in moiré flat bands, *Nat. Phys.* **16**, 725 (2020).
- [6] Y. Cao, V. Fatemi, A. Demir, S. Fang, S. L. Tomarken, J. Y. Luo, J. D. Sanchez-Yamagishi, K. Watanabe, T. Taniguchi, E. Kaxiras *et al.*, Correlated insulator behaviour at half-filling in magic-angle graphene superlattices, *Nature (London)* **556**, 80 (2018).
- [7] G. Chen, L. Jiang, S. Wu, B. Lyu, H. Li, B. L. Chittari, K. Watanabe, T. Taniguchi, Z. Shi, J. Jung *et al.*, Evidence of a gate-tunable Mott insulator in a trilayer graphene moiré superlattice, *Nat. Phys.* **15**, 237 (2019).
- [8] Y. Jiang, X. Lai, K. Watanabe, T. Taniguchi, K. Haule, J. Mao, and E. Y. Andrei, Charge order and broken rotational symmetry

- in magic-angle twisted bilayer graphene, *Nature (London)* **573**, 91 (2019).
- [9] A. Kerelsky, L. J. McGilly, D. M. Kennes, L. Xian, M. Yankowitz, S. Chen, K. Watanabe, T. Taniguchi, J. Hone, C. Dean *et al.*, Maximized electron interactions at the magic angle in twisted bilayer graphene, *Nature (London)* **572**, 95 (2019).
- [10] Y. Cao, D. Rodan-Legrain, J. M. Park, F. N. Yuan, K. Watanabe, T. Taniguchi, R. M. Fernandes, L. Fu, and P. Jarillo-Herrero, Nematicity and competing orders in superconducting magic-angle graphene, *Science* **372**, 264 (2021).
- [11] U. Zondiner, A. Rozen, D. Rodan-Legrain, Y. Cao, R. Queiroz, T. Taniguchi, K. Watanabe, Y. Oreg, F. von Oppen, A. Stern *et al.*, Cascade of phase transitions and Dirac revivals in magic-angle graphene, *Nature (London)* **582**, 203 (2020).
- [12] D. Wong, K. P. Nuckolls, M. Oh, B. Lian, Y. Xie, S. Jeon, K. Watanabe, T. Taniguchi, B. A. Bernevig, and A. Yazdani, Cascade of electronic transitions in magic-angle twisted bilayer graphene, *Nature (London)* **582**, 198 (2020).
- [13] G. Chen, A. L. Sharpe, E. J. Fox, Y.-H. Zhang, S. Wang, L. Jiang, B. Lyu, H. Li, K. Watanabe, T. Taniguchi *et al.*, Tunable correlated Chern insulator and ferromagnetism in a moiré superlattice, *Nature (London)* **579**, 56 (2020).
- [14] M. Serlin, C. L. Tschirhart, H. Polshyn, Y. Zhang, J. Zhu, K. Watanabe, T. Taniguchi, L. Balents, and A. F. Young, Intrinsic quantized anomalous Hall effect in a moiré heterostructure, *Science* **367**, 900 (2020).
- [15] H. C. Po, L. Zou, A. Vishwanath, and T. Senthil, Origin of Mott Insulating Behavior and Superconductivity in Twisted Bilayer Graphene, *Phys. Rev. X* **8**, 031089 (2018).
- [16] Z. Song, Z. Wang, W. Shi, G. Li, C. Fang, and B. A. Bernevig, All Magic Angles in Twisted Bilayer Graphene are Topological, *Phys. Rev. Lett.* **123**, 036401 (2019).
- [17] J. Kang and O. Vafek, Symmetry, Maximally Localized Wannier States, and a Low-Energy Model for Twisted Bilayer Graphene Narrow Bands, *Phys. Rev. X* **8**, 031088 (2018).
- [18] N. F. Q. Yuan and L. Fu, Model for the metal-insulator transition in graphene superlattices and beyond, *Phys. Rev. B* **98**, 045103 (2018).
- [19] F. Wu, T. Lovorn, E. Tutuc, and A. H. MacDonald, Hubbard Model Physics in Transition Metal Dichalcogenide moiré Bands, *Phys. Rev. Lett.* **121**, 026402 (2018).
- [20] Y. Zhang, N. F. Q. Yuan, and L. Fu, Moiré quantum chemistry: Charge transfer in transition metal dichalcogenide superlattices, *Phys. Rev. B* **102**, 201115(R) (2020).
- [21] L. Wang, E.-M. Shih, A. Ghiotto, L. Xian, D. A. Rhodes, C. Tan, M. Claassen, D. M. Kennes, Y. Bai, B. Kim *et al.*, Correlated electronic phases in twisted bilayer transition metal dichalcogenides, *Nat. Mater.*, **19**, 861 (2020).
- [22] E. C. Regan, D. Wang, C. Jin, M. I. B. Utama, B. Gao, X. Wei, S. Zhao, W. Zhao, Z. Zhang, K. Yumigeta *et al.*, Mott and generalized Wigner crystal states in WSe₂/WS₂ moiré superlattices, *Nature (London)* **579**, 359 (2020).
- [23] Y. Xu, S. Liu, D. A. Rhodes, K. Watanabe, T. Taniguchi, J. Hone, V. Elser, K. F. Mak, and J. Shan, Correlated insulating states at fractional fillings of moiré superlattices, *Nature (London)* **587**, 214 (2020).
- [24] T. Li, S. Jiang, L. Li, Y. Zhang, K. Kang, J. Zhu, K. Watanabe, T. Taniguchi, D. Chowdhury, L. Fu, J. Shan, and K. F. Mak, Continuous Mott transition in semiconductor moiré superlattices, *Nature* **597**, 350 (2021).
- [25] S. Doniach, The Kondo lattice and weak antiferromagnetism, *Physica B+C* **91**, 231 (1977).
- [26] F. Steglich, J. Aarts, C. D. Bredl, W. Lieke, D. Meschede, W. Franz, and H. Schäfer, Superconductivity in the Presence of Strong Pauli Paramagnetism: CeCu₂Si₂, *Phys. Rev. Lett.* **43**, 1892 (1979).
- [27] S. G. R. Stewart, Heavy-fermion systems, *Rev. Mod. Phys.* **56**, 755 (1984).
- [28] S. Nakatsuji and Y. Maeno, Quasi-Two-Dimensional Mott Transition System Ca_{2-x}Sr_xRuO₄, *Phys. Rev. Lett.* **84**, 2666 (2000).
- [29] V. I. Anisimov, I. A. Nekrasov, D. E. Kondakov, T. M. Rice, and M. Sigrist, Orbital-selective Mott-insulator transition in Ca_{2-x}Sr_xRuO₄, *Eur. Phys. J. B* **25**, 191 (2002).
- [30] H. Löhneysen, S. Mock, A. Neubert, T. Pietrus, A. Rosch, A. Schröder, O. Stockert, and U. Tutsch, Heavy-fermion systems at the magnetic-nonmagnetic quantum phase transition, *J. Magn. Magn. Mater.* **177**, 12 (1998).
- [31] H. von Löhneysen, Non-Fermi-liquid behaviour in the heavy-fermion system, *J. Phys.: Condens. Matter* **8**, 9689 (1996).
- [32] H. Von Löhneysen, A. Neubert, T. Pietrus, A. Schröder, O. Stockert, U. Tutsch, M. Loewenhaupt, A. Rosch, and P. Wölfle, Magnetic order and transport in the heavy-fermion system Ce-CuAu, *Eur. Phys. J. B* **5**, 447 (1998).
- [33] A. Schröder, G. Aeppli, R. Coldea, M. Adams, O. Stockert, H. Löhneysen, E. Bucher, R. Ramazashvili, and P. Coleman, Onset of antiferromagnetism in heavy-fermion metals, *Nature (London)* **407**, 351 (2000).
- [34] T. Senthil, S. Sachdev, and M. Vojta, Fractionalized Fermi Liquids, *Phys. Rev. Lett.* **90**, 216403 (2003).
- [35] G. R. Stewart, Non-fermi-liquid behavior in *d*- and *f*-electron metals, *Rev. Mod. Phys.* **73**, 797 (2001).
- [36] J. Custers, P. Gegenwart, H. Wilhelm, K. Neumaier, Y. Tokiwa, O. Trovarelli, C. Geibel, F. Steglich, C. Pépin, and P. Coleman, The break-up of heavy electrons at a quantum critical point, *Nature (London)* **424**, 524 (2003).
- [37] T. Senthil, M. Vojta, and S. Sachdev, Weak magnetism and non-Fermi liquids near heavy-fermion critical points, *Phys. Rev. B* **69**, 035111 (2004).
- [38] P. Coleman, Heavy fermions: Electrons at the edge of magnetism, in *Handbook of Magnetism and Advanced Magnetic Materials*, edited by Ekkes Brück (Elsevier, New York, 2007).
- [39] P. Gegenwart, Q. Si, and F. Steglich, Quantum criticality in heavy-fermion metals, *Nat. Phys.* **4**, 186 (2008).
- [40] M. Vojta, Orbital-selective Mott transitions: Heavy fermions and beyond, *J. Low Temp. Phys.* **161**, 203 (2010).
- [41] H. Q. Yuan, F. M. Grosche, M. Deppe, C. Geibel, G. Sparn, and F. Steglich, Observation of two distinct superconducting phases in CeCu₂Si₂, *Science* **302**, 2104 (2003).
- [42] D. Aoki, K. Ishida, and J. Flouquet, Review of *u*-based ferromagnetic superconductors: Comparison between UGe₂, URhGe, and UCoGe, *J. Phys. Soc. Jpn.* **88**, 022001 (2019).
- [43] L. Jiao, S. Howard, S. Ran, Z. Wang, J. O. Rodriguez, M. Sigrist, Z. Wang, N. P. Butch, and V. Madhavan, Chiral superconductivity in heavy-fermion metal UTe₂, *Nature (London)* **579**, 523 (2020).
- [44] G.-B. Liu, W.-Yu Shan, Y. Yao, W. Yao, and Di Xiao, Three-band tight-binding model for monolayers of group-VIB transition metal dichalcogenides, *Phys. Rev. B* **88**, 085433 (2013).

- [45] S. Biermann, L. deMedici, and A. Georges, Non-Fermi-Liquid Behavior and Double-Exchange Physics in Orbital-Selective Mott Systems, *Phys. Rev. Lett.* **95**, 206401 (2005).
- [46] S. Florens and A. Georges, Slave-rotor mean-field theories of strongly correlated systems and the Mott transition in finite dimensions, *Phys. Rev. B* **70**, 035114 (2004).
- [47] E. Zhao and A. Paramekanti, Self-consistent slave rotor mean-field theory for strongly correlated systems, *Phys. Rev. B* **76**, 195101 (2007).
- [48] C. Chen, I. Sodemann, and P. A. Lee, Competition of spinon Fermi surface and heavy Fermi liquids states from the periodic anderson to the Hubbard model, *Phys. Rev. B* **103**, 085128 (2021).
- [49] S.-M. Huang, Y.-P. Huang, and T.-K. Lee, Slave-rotor theory on magic-angle twisted bilayer graphene, *Phys. Rev. B* **101**, 235140 (2020).
- [50] This shift can be absorbed into $\bar{\epsilon}_\tau$.
- [51] A. Laturia, M. L. Van de Put, and W. G. Vandenberghe, Dielectric properties of hexagonal boron nitride and transition metal dichalcogenides: From monolayer to bulk, *npj 2D Mater. Appl.* **2**, 6 (2018).
- [52] We neglect the angle dependence of U .
- [53] One should note the regions where the densities of the different species are locked to the value $n_\tau = 2$. These regions correspond to a band insulator in the relevant species, where the corresponding band is completely filled with two particles per moiré unit cell.
- [54] A. Keselman, L. Savary, and L. Balents, Dimer description of the Su(4) antiferromagnet on the triangular lattice, *SciPost Phys.* **8**, 076 (2020).
- [55] A. Keselman, B. Bauer, C. Xu, and C.-M. Jian, Emergent Fermi Surface in a Triangular-Lattice Su(4) Quantum Antiferromagnet, *Phys. Rev. Lett.* **125**, 117202 (2020).
- [56] F. Wu, T. Lovorn, E. Tutuc, I. Martin, and A. H. MacDonald, Topological Insulators in Twisted Transition Metal Dichalcogenide Homobilayers, *Phys. Rev. Lett.* **122**, 086402 (2019).
- [57] Y.-H. Zhang, D. N. Sheng, and A. Vishwanath, An Su(4) chiral spin liquid and quantized dipole Hall effect in moiré bilayers, [arXiv:2103.09825](https://arxiv.org/abs/2103.09825).
- [58] B. Fischer and M. W. Klein, Magnetic and nonmagnetic impurities in two-dimensional metals, *Phys. Rev. B* **11**, 2025 (1975).
- [59] We note that this transition line will be pushed to larger θ_M upon increase of the interaction parameter U .
- [60] A. Rozen, J. M. Park, U. Zondiner, Y. Cao, D. Rodan-Legrain, T. Taniguchi, K. Watanabe, Y. Oreg, A. Stern, E. Berg, P. Jarillo-Herrero, and S. Ilani, Entropic evidence for a Pomeranchuk effect in magic-angle graphene, *Nature* **592**, 214 (2021).
- [61] Yu Saito, F. Yang, J. Ge, X. Liu, K. Watanabe, T. Taniguchi, J. I. A. Li, E. Berg, and A. F. Young, Isospin Pomeranchuk effect and the entropy of collective excitations in twisted bilayer graphene, *Nature (London)* **592**, 220 (2021).
- [62] A. Joshua, S. Pecker, J. Ruhman, E. Altman, and S. Ilani, A universal critical density underlying the physics of electrons at the LaAlO₃/SrTiO₃ interface, *Nat. Commun.* **3**, 1129 (2012).
- [63] S. Ilani, A. Yacoby, D. Mahalu, and H. Shtrikman, Unexpected Behavior of the Local Compressibility Near the $b = 0$ Metal-Insulator Transition, *Phys. Rev. Lett.* **84**, 3133 (2000).
- [64] B. Fallahazad, H. C. P. Movva, K. Kim, S. Larentis, T. Taniguchi, K. Watanabe, S. K. Banerjee, and E. Tutuc, Shubnikov-De Haas Oscillations of High-Mobility Holes in Monolayer and Bilayer WSe₂: Landau Level Degeneracy, Effective Mass, and Negative Compressibility, *Phys. Rev. Lett.* **116**, 086601 (2016).
- [65] A. Ramires and J. L. Lado, Emulating Heavy Fermions in Twisted Trilayer Graphene, *Phys. Rev. Lett.* **127**, 026401 (2021).
- [66] H. Li, S. Li, M. H. Naik, J. Xie, X. Li, E. Regan, D. Wang, W. Zhao, K. Yumigeta, M. Blei, T. Taniguchi, K. Watanabe, S. Tongay, A. Zettl, S. G. Louie, M. F. Crommie, and F. Wang, Imaging local discharge cascades for correlated electrons in WS₂/WSe₂ moiré superlattices, *Nat. Phys.* **17**, 1114 (2021).
- [67] A. C. Hewson, *The Kondo Problem to Heavy Fermions* (Cambridge University Press, Cambridge, England, 1997), Vol. 2.